IEEE Journal of Translational Engineering in Health and Medicine

Received 8 October 2017; revised 11 January 2018 and 12 February 2018; accepted 2 March 2018.
Date of publication 22 March 2018; date of current version 2 April 2018.

Digital Object Identifier 10.1109/JTEHM.2018.2818177

Precision of EM Simulation Based Wireless Location Estimation in Multi-Sensor Capsule Endoscopy

UMAIR KHAN[1,2], YUNXING YE[3], AIN-UL-AISHA[4], PRANAY SWAR[5], AND KAVEH PAHLAVAN[1]

[1]Worcester Polytechnic Institute, Worcester, MA 01609, USA
[2]Intel Corporation, Hudson, MA 01749, USA
[3]Audi of America, Belmont, CA 94002, USA
[4]Hitachi Vantara, Waltham, MA 02451, USA
[5]AirWatch, Sandy Springs, GA 30338, USA

CORRESPONDING AUTHOR: U. KHAN (umiar.ishaq@gmail.com)

ABSTRACT In this paper, we compute and examine two-way localization limits for an RF endoscopy pill as it passes through an individuals gastrointestinal (GI) tract. We obtain finite-difference time-domain and finite element method-based simulation results position assessment employing time of arrival (TOA). By means of a 3-D human body representation from a full-wave simulation software and lognormal models for TOA propagation from implant organs to body surface, we calculate bounds on location estimators in three digestive organs: stomach, small intestine, and large intestine. We present an investigation of the causes influencing localization precision, consisting of a range of organ properties; peripheral sensor array arrangements, number of pills in cooperation, and the random variations in transmit power of sensor nodes. We also perform a localization precision investigation for the situation where the transmission signal of the antenna is arbitrary with a known probability distribution. The computational solver outcome shows that the number of receiver antennas on the exterior of the body has higher impact on the precision of the location than the amount of capsules in collaboration within the GI region. The large intestine is influenced the most by the transmitter power probability distribution.

INDEX TERMS Endoscopy pill, TOA location limits, bounds, 3D, two-way location, signal probability.

I. INTRODUCTION

Lately, wireless capsule endoscopy (WCE) has garnered plenty of interest owing to its non-intrusive characteristic [1]. Assessment of the gastro-intestinal (GI) region is essential to recognize any colorectal cancer inside the digestive system tract. It has been discovered that colorectal cancer is the second foremost source of cancer associated fatalities in the United States. Additionally, WCE permits the doctor to depict the whole GI region exclusive of scope trauma and air insufflations. Conventional practices like gastroscopy and colonoscopy can barely get to the first couple of or final few feet of the GI region.

The WCE obtained its endorsement from the U.S. Food and Drug Administration (FDA) in 2001, and in excess of 200,000 patients have taken advantage of the benefits of this innovative skill. WCE begins with the subject ingesting the pill. The normal motion of muscles transports the pill effortlessly and simply all through the GI tract, which is sending out color picture taken by the camera in the pill as it goes through. The process is mobile, permitting the subjects to carry on with their every day activity all through the endoscopic assessment. In spite of the benefits WCE has, it is reported that a doctor takes a couple hours to review the snapshots taken through every WCE assessment, given that roughly fifty thousand pictures are taken throughout the eight hour timeframe of the test [2]. This reduces the speed of this method of assessment and makes the process considerably more expensive. Besides, after the assessment by WCE, the doctor might have a desire to re-examine a location of concern for additional analysis or management.

Precise position data of the pill can assist in both quickening up the review of the snapshots and supporting the doctor for eventual treatment.

A variety of methods for positioning of the pill have been researched in viability analyses. The initial plan was to employ a spatial examining scheme to establish the position of the points with the highest received signal strength (RSS). This method is unmarketable and unmanageable.

Frisch *et al.* [3] examined a wireless triangulation scheme by means of an exterior antenna arrangement that gauges the signal power of the pills communications at several positions and applies this data to approximate the space between the pill and external sensors. The mean investigational inaccuracy is described to be 37.7 mm [4]. A technique put forth by Kuth *et al.* [5] to estimate the location and direction of the pill using X-ray emission photography. The method results in the pill to be be seen explicitly because it possesses a number of energy impervious features that are typically made of metal or synthetic material and exhibit a an extremely distinct photograph. Hence, it is conceivable to function with a very little amount of energy helping in decreasing medical hazards on the subjects. Another process was suggested by Kawasaki and Kohno [6] to pinpoint the position of biological implants by means of TOA established waveform recovery technique. Initially, the transmission velocity of the waveform propagating in the patients body is approximated by collecting the photographs from CAT or MRI machines. After that, a dynamic pattern fusion technique is used to compute the transmission period established by the result of the comparator in the middle of the Tx and the Rx. Additional methods established for the positioning of camera pills comprise magnetic field detection [7]. A tiny permanent magnet is encased into the pill. With the detection information of a magnetic antenna arrangement on the exterior the subjects body, the 3D positioning and 2D direction of the pill are approximated. More recently some studies like [8] and [9], have employed hybrid localizations using data fusion of vision and RF sensors for WCE applications. Accelerometer based techniques have also been employed in camera pill positioning [10], [11]. In this research, a 39.3 mm electronic inertial meter with three axes, operating at 20 Hz, was inserted inside the pill and information was propagated using Zigbee protocol to an outside workstation. Because the inertia is quantitatively obtained, velocity can be calculated more precisely than location as it needs only one integral solution. Therefore, classifying the actual position of each image obtained from the pill is important in both analytic and remedial purposes of pill based endoscopy.

One of the most popular methodologies, RSS based positioning techniques have the benefit of versatility and a comparatively small price of execution. Consequently, it has been selected to be employed for the Smartpill device [12] in USA and the M2A device [13] in Israel. Usually, wireless positioning methods use results obtained from TOA, angle of arrival (AOA) or RSS experiments. Even though, the RSS method is less sensitive to a restricted frequency spectrum and inhospitable wireless channels, a commonly acknowledged advantage of the TOA method is better precision relative to the RSS and AOA methods [14], despite some studies like [15] attempting to combine these two techniques for better precision. Nonetheless, the high refractive index of the body results in sizable inaccuracies in TOA approximation and the restricted frequency band (402–405 MHz) of Medical Implant Communication Services (MICS) makes it difficult to perform precise TOA measurements. This issue is worsened by the motion of the GI tract, and the drainage and replenishing sequence, resultant in irregular errors in distance measurements [16]. Hence, the location data from TOA approximation is not optimal in the existing literature; and this paper attempts to remedy this problem.

There are essentially two methods to employ TOA data for positioning, triangulation and waveform identification. In this study, we limit our focus on the problems concerned with TOA triangulation methods. The TOA Triangulation method is derived from the impulse response model from organs containing the devices to the exterior of the body. The technique is employed to compute the space between every surface antenna and the pill. After that, at least four of the measured distances are employed to compute the position of the pill in 3D space.

The most difficult issue in the positioning of the pill arises from the complicated nature of the surroundings of the pill as it goes down the human body. Because the GI tract is of an extended cylindrical formation that doubles up on its own at multiple instances and has the freedom to shift inside the abdomen, it is very challenging to precisely determine the position of the pill. Adding to that, because of the subject moving about and resting activities like breathing, the actual position of the antennas on the exterior of the patient and their comparative location to the pill within the GI tract keeps changing, deeming the meaning of positioning dissimilar from conventional definitions. At present, the majority of studies have concentrated on coming up with algorithms and mathematical models to find the solution of the triangulation issue section III in [17]. In this paper, we take a separate route. Basing our approach on the statistical medical device impulse response model derived in [18], we concentrate on the precision of pills traveling inside the body using TOA based triangulation methods; Yi *et al.* have derived the positioning bound computation for a solitary capsule scenario in [19]. The Cramer-Rao bounds (CRB) developed in this study measure the restrictions of positioning precision with multiple external sensor protocol, medical device impulse response method and multiple capsules inside the body. Our end goal is to investigate the precision attainable at different tissues and decide whether this precision is sufficient for WCE. Related papers have been published for indoor personnel localization [20] and robot positioning [21].

We start in Section. II by detailing the computer aided finite element method (FEM) simulations describe the environment and the device to exterior impulse response model for the human body. After that, employing the exact position

IEEE Journal of Translational Engineering in Health and Medicine

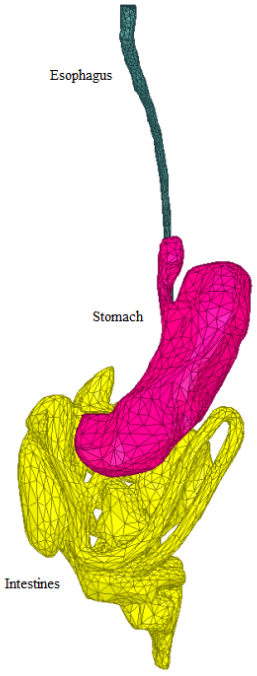

FIGURE 1. An Illustration of the human digestive system the typical path of an endoscopy pill.

obtained form the CAD design and the mathematical model, we obtain the CRB for multiple pill positioning and the positioning bound with arbitrariness in the signal timing in Section. III. In Section IV, we present outcomes of the model that emphasize the sensor and tissue position factors that influence the precision of positioning. We test the accuracy of the computational solver used in this study in Section V. In the end, we offer our conclusions in Section VI.

II. FUNCTIONALITY AND ASSESSMENT APPROACH

A. FUNCTIONALITY ASSESSMENT SETUP

A human digestive system is made up of an intestines, a stomach and an esophagus, as illustrated in Fig. 1. To effectively construct a model setup to compute the CRB of an RF endoscopy pill as it moves down the GI tract, we employ a three-dimensional body simulation from the 3D FEM based high-frequency solver (HFSS [22]). We establish the accuracy of this solver by comparing basic field measurements with their corresponding simulation models in HFSS. For research purposes we use a center frequency of 900MHz with a bandwidth of 100MHz. Each simulation run took about 4-6 hours to complete. Further details of these scenarios are presented in Section V.

This simulation has a 2mm 3-D resolution and comprises of radio-wave permeability characteristics of over 175 organs of a female human body. From this we obtain spatial positions of the GI tract, as shown in Fig. 2. For the positioning of the external antennas, we implemented the scenario in [3] and [23], with the assumption that these antennas are positioned on a vest worn by the subject for the duration of the investigation. Matching quantities of sensors are placed in the anterior and on the posterior of the vest. We computed the CRB for 8, 16, 32 and 64 external antennas with a spatial position of 268, 9, 323, 9, 312 mm, a representative arrangement for 32 external antennas is demonstrated in Fig. 3.

B. TOA MODEL FOR THE DIGESTIVE SYSTEM

In this section, we outline the internal sensor to external sensor mathematical TOA model that is employed to compute the CRB of endoscopy pill positioning. This model makes use of the signal velocity model in different dielectric materials and described in [18]. The key elements employed to establish this model comprise the FEM based simulation engine and human body model from Ansys. The TOA between the internal and external sensor antennas can be calculated using the following equation:

$$\nu(\omega) = \frac{c}{\sqrt{\epsilon_r(\omega)}}, \tag{1}$$

where $\nu(\omega)$ is the velocity of the signal in a human tissue, c is the velocity of a radio signal is space, and ϵ_r is the dielectric constant of the human tissue. As stated before, biological materials highly attenuate a radio wave. Hence, a very high dielectric constant is estimated. In our simulations, we employ a 100 mm displacement between external and internal sensors as the limit for selecting the dielectric constant. If the displacement is lower than 100 mm, we pick the near surface dielectric constant, in other cases deep tissue dielectric constants are used. An example of surface-to-surface communication can be seen in can be seen in Fig. 5. Fig. 4 shows a plot obtained from this equation. Note that it will not give us a linear distribution of values for distance for each time of arrival. We will therefore have to add a random variable and calculate bounds on its standard distributions in our computations.

The standard deviation for this random variable can be represented by

$$\sigma_D^2 \geq \frac{1}{8\pi^2}\frac{1}{SNR}\frac{1}{TW}\frac{1}{f_0^2}\frac{1}{1+\frac{W^2}{12f_0^2}}, \tag{2}$$

where T is the observation time, SNR is the Signal-To-Noise-Ratio. f_0 is the center frequency of operation and W is the bandwidth of the system.

C. UNPREDICTABILITY OF IMPULSE TIME ARRIVAL

In real-life wireless system scenarios, the antennas cannot predict an accurate time of arrival of the pulse because of the price of the standard calibration of the apparatus. While, the measure time of arrival may be a particular nanosecond value, the arrival time fluctuates a small number of nanoseconds around the this mean [24]. The chief elements that affect time of arrival deviation for networks in and around the human body are enumerated thus: (a) apparatus assembly disparity and differences in battery levels from one node to the other, (b) motion of the patient subject because of movements

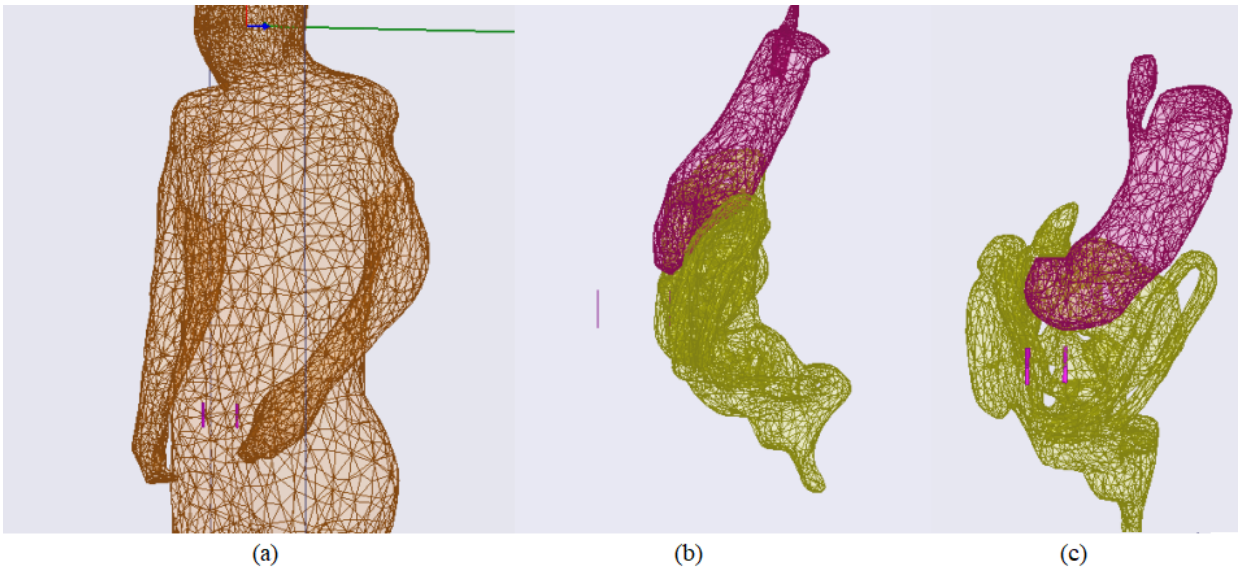

FIGURE 2. Positions of one internal and one external sensor as seen from (a) slightly turned outside the body (b) side of the stomach and intestines (c) slightly turned stomach and intestine.

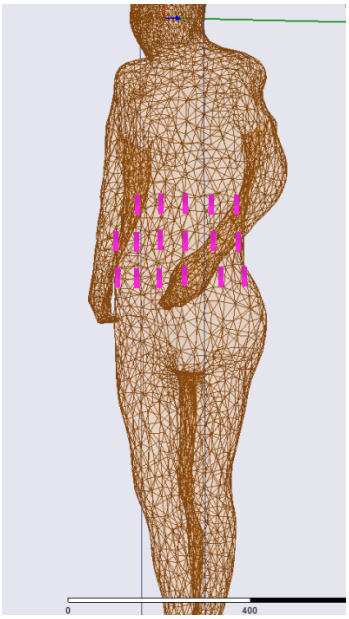

FIGURE 3. External Sensor Distribution (note: an equal number of sensors would be placed on the opposite side of the model).

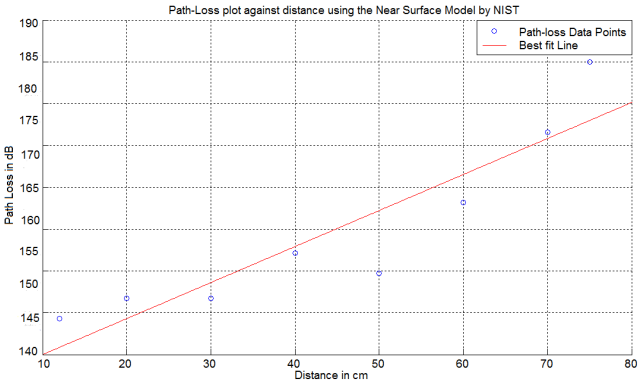

FIGURE 4. Plot obtained from eq. (1).

and variations in the directions of the sensors, (c) the node devices may not be located at the exact height above from the body exterior at the same time. Some sensors could be in contact with the exterior while some may be a little ways above the surface. As stated in [25], a time than the sensor not in contact with human tissue. All these elements add to the uncertainty in the time of arrival of the pulse which in turn has an impact on the precision of positioning.

III. TOA SIMULATIONS AND OBSERVATIONS

Fig. 2 shows an FEM simulation in HFSS and Fig. 6 *shows* the waveform received at the sensor on the surface of the belly with the transmitter positioned inside the small intestine. The transmitter and receiver are about 11 *cm* apart. As shown in the time domain response (TDR) plot in Fig. 6, the pulse is received at 0.48 ns, which roughly translates to 14.4 cm, i.e. a distance measurement error of 3.4 cm. Notice, also, in Fig. 2 that the dipoles are modeled to act as both the pill and surface sensors for the simulations. This is for simplicity of design, and to reduce simulation time and computational resources needed. The downside of using these dipoles to represent the sensors is the capacitive dip we see before and after the received pulse in the waveform. But if we plot the normalized power received, the negative region of that plot will be eliminated when the voltage is squared.

A number of such simulations were carried out with the transmitter kept in the intestine and the position of the receiver was rotated around the body at 10 different positions at the same horizontal level, to account for different distances. One such simulation was run where the position of the

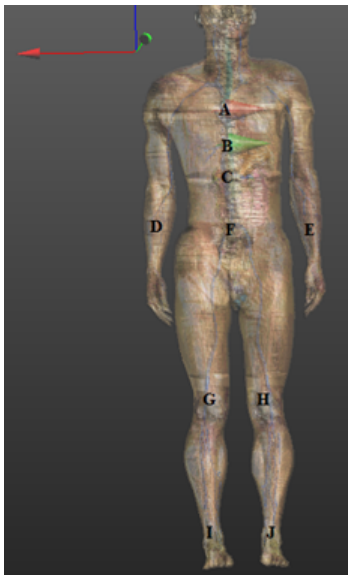

FIGURE 5. An example of surface-surface communication.

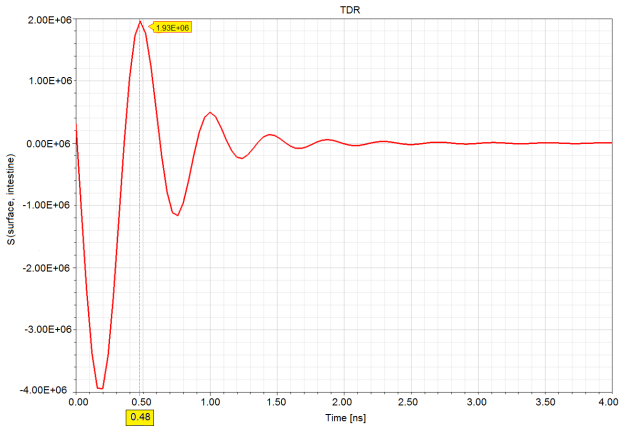

FIGURE 6. Impulse response between pill inside intestine and sensor on the surface of the belly.

transmitter was in the intestine and the receiver was kept at the same horizontal position but at the models back, to see what happens when the waveform travels through bones and other tissue on its way from one sensor to another. This verifies the shadow-fading effect due to the higher density of organs between the two sensors. Fig. 7 illustrates what the waveform looks like after passing through these denser tissue.

All these simulations were then used to plot a distance vs. TOA plot to assess deviations of the plotted points from a straight line representing the ideal TOA for each distance. Fig. 8 shows this plot.

The standard deviation per dB of the Path-loss model, from the PDF shown in Figure 12, came out to be $15.575/50 = 0.3115$. While, the standard deviation per ns of the TOA model, form the PDF shown in Fig. 10, came out to be $0.361004/1.4 = 0.25786$. Hence, the TOA model seems to be more accurate. More detailed simulations are underway to improve the accuracy of the TOA model.

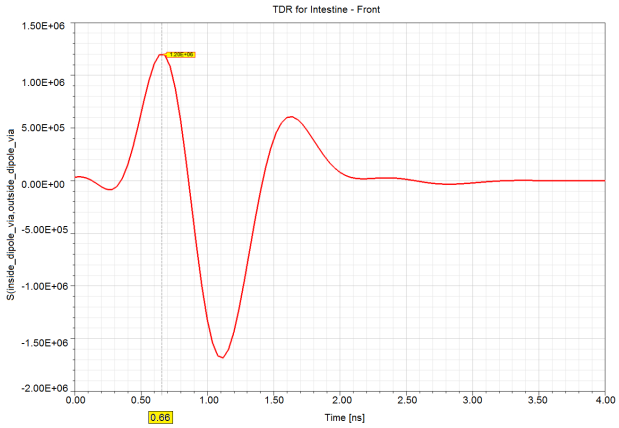

FIGURE 7. Impulse response between pill inside intestine and sensor on the back.

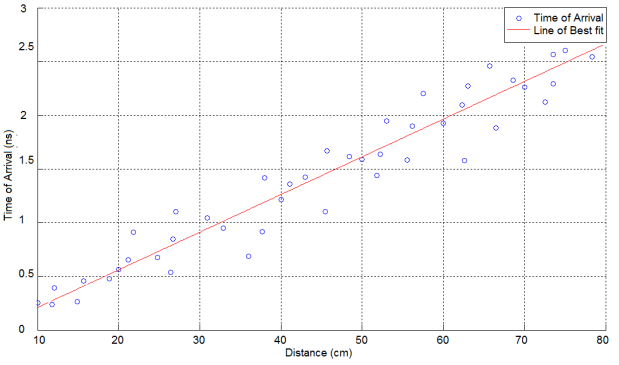

FIGURE 8. Time of Arrival vs. distance for various sensor positions.

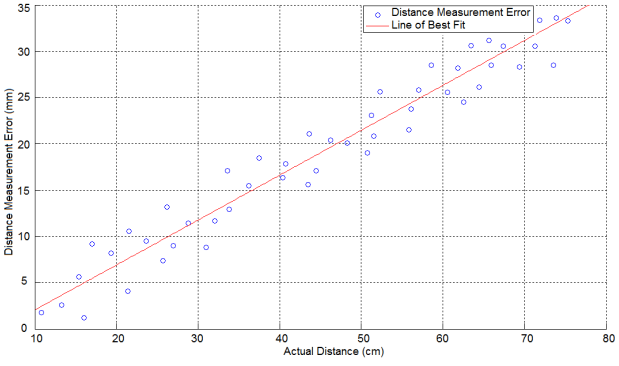

FIGURE 9. Distance Measurement Error from TOA for each sensor position.

To estimate the distance from the TOA plot shown in Fig.8, we used eq. (1).

From the slope of the TOA vs. distance line, the ϵ_r came out to be 1.336. This value was also used to estimate the measured value for a distance of 5 cm between the sensors, mentioned in section IV. Fig. 9 shows the distance measurement error plot obtained from the simulations carried out. It can be seen that the distance measurement error (given in millimeters) increases linearly with distance.

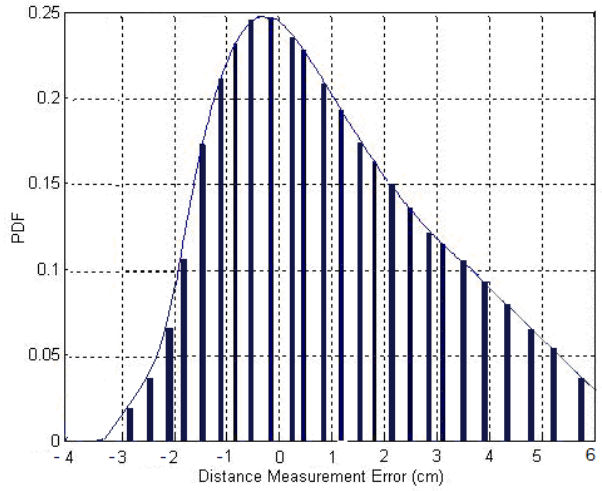

FIGURE 10. PDF of the Distance Measurement Error from TOA for each sensor position.

IV. CRB FOR TOA BASED SPATIAL ENDOSCOPY PILL POSITIONING

In this section, we develop the spatial CRB established on the TOA models described in the preceding section. We take into account both scenarios with multiple sensors are in working together and where there is variations in pulse arrival times. The CRB for 2D positioning limits has been discussed in [26]. Here, we describe the limits in all three spatial dimensions by working on the calculations done in two dimensions.

A. CRB FOR MULTI-SENSOR COLLABORATIVE POSITIONING

Extending on the TOA models in Section. II, we will perform derivations for the spatial CRB for collaborative positioning of an endoscopy pill. We study the following setup: N RF sensor nodes are positioned on the surface of the human body using the vest with the position of each represented by $\theta_c = [p_2, p_2, \ldots, p_N]$. The path of these sensors from the capsule could be blocked but they can quantify the TOA their adjacent nodes and the most visible sensor can receive the TOA data from the capsule and perform additional computation in collaboration with the other sensors. M number of capsules could be swallowed by the patient subject with their positions represented by $\theta_r = [p_{N+1}, \ldots, p_{N+M}]$. The vector of sensor factors is $\theta = [\theta_c \theta_r]$. For this spatial scenario, $p_i = [x_i, y_i, z_i]^T$ where $i \in [1, N+M]$ and T is the transpose action. The unidentified elements to be calculated may be denoted by a $3 \times N$ matrix.

$$\begin{aligned}\theta_c &= [p_1, p_2, \ldots, p_N], \\ &= \begin{bmatrix} x_1 & x_2 & \ldots & x_N \\ y_1 & y_2 & \ldots & y_N \\ z_1 & z_2 & \ldots & z_N \end{bmatrix}. \end{aligned} \tag{3}$$

Take the sensors into consideration (sensors comprise the pill and surface antennas).i and j receive paired-up signals X_{ij}. We make the assumption that all surface antennas can detect the TOA from the pill travelling through the GI tract, but the multi-path characteristics for the various transmission paths change as the number of different media between the surface antenna and the pill travelling down the GI tract varies. Hence, we take $H\{i\} = \{j;$ sensor j receives linked-up signals from sensor i$\}$. $H\{i\} = \{1, \ldots, i\,1, i+1, \ldots N+M\}$ for $i \in [1, N]$ and $H\{i\} = \{1, N\}$ for $i \in [N+1, N+M]$ since a sensor is not able to receive a linked signal from itself and the surface antennas will not receive signals from other receivers either. Thus, the size of the received vector X is $N \times (N + M1) + M \times N$.

Using mutuality, we make the assumption $X_{ij} = X_{ji}$, therefore, it is enough to study just the lower vertex of the receiver matrix X when expressing the combined probability function [27]. The CRB on the covariance matrix of any unbiased estimator $\hat{\theta}$ is given by [28]:

$$cov(\hat{\theta}) = E\big[(\hat{\theta} - \theta)(\hat{\theta} - \theta)^T\big] \geq F_\theta^{-1}, \tag{4}$$

where $E[\cdot]$ is the expectation operation and F is the Fisher information matrix (FIM) defined as:

$$\begin{aligned} F_\theta &= -E\nabla_\theta(\nabla_\theta \ln f(X|\theta))^T, \\ &= E_\theta[\frac{\partial}{\partial\theta}\ln f(X|\theta)\big(\frac{\partial}{\partial\theta}\ln f(X|\theta)\big)^T], \\ &= \begin{bmatrix} F_{R_{XX}} & F_{R_{XY}} & F_{R_{XZ}} \\ F_{R_{XY}}^T & F_{R_{YY}} & F_{R_{YZ}} \\ F_{R_{XZ}}^T & F_{R_{YZ}}^T & F_{R_{ZZ}} \end{bmatrix} \text{3D situation} \end{aligned} \tag{5}$$

where $f(X|\theta)$ is the joint PDF of the observation vector X conditioned on θ. For the RSS measurements case, the $X_{i,j}$ are log-normal random variables, and the density is given by [19]

$$\begin{aligned} f(X_{i,j}|p_i, p_j) &= \frac{\frac{10}{\log 10}}{\sqrt{2\pi\sigma_{dB}^2}}\frac{1}{X_{i,j}}\exp\Big[-\frac{b}{8}\big(\log\frac{d_{i,j}^2}{\tilde{d}_{i,j}^2}\big)^2\Big] \\ b &= \Big(\frac{10\alpha}{\sigma_{dB}}\Big)^2, \\ \tilde{d}_{i,j} &= d_0\Big(\frac{X_0}{X_{i,j}}\Big)^{\frac{1}{x}}, \\ d_{i,j} &= \sqrt{(x_i - x_j)^2 + (y_i - y_j)^2 + (z_i - z_j)^2} \end{aligned} \tag{6}$$

for $i = 1, 2, N+M$ and $j \in H(i)$, $\mathfrak{d}(i,j)$ is the MLE of range $d_{i,j}$ given received power X_{ij}. Then the logarithm of the joint condition pdf is

$$l(X|\theta) = \sum_{i=1}^{M+N}\sum_{j\in H_{i,j}<i}\log f_{X|\theta}(X_{i,j}|p_i, p_j). \tag{7}$$

It is mentioned in [26] that the second-order partial differential of eq. (7) w.r.t θ_r and θ_s is going to be a total of terms if θ_r and θ_s are coordinates of the same sensor k, but will be only one term if θ_r and θ_s are coordinates of separate sensors

k and l, $k \neq l$. For example:

$$\frac{\partial^2 l(X|\theta)}{\partial x_k \partial z_k} = -b \sum_{i \in H(k)} \frac{(x_i - x_k)(z_i - z_k)}{d_{i,k}^4} \Big[-\log \frac{d_{i,k}^2}{\tilde{d}_{i,k}^2} - 1 \Big],$$
$$\frac{\partial^2 l(X|\theta)}{\partial x_k \partial z_l} = -b I_{H(k)}(l) \frac{(x_i - x_k)(z_i - z_k)}{d_{i,k}^4} \Big[\log \frac{d_{i,k}^2}{\tilde{d}_{i,k}^2} - 1 \Big], \tag{8}$$

where $I_{H(k)(l)} = 1$ if $l \in H(k)$ and 0 otherwise. since $E\big(\frac{d_{i,k}^2}{\tilde{d}_{i,k}^2}\big) = 0$. Thus the elements of F_θ are:

$$[F_{R_{XX}}]_{k,l} = \begin{cases} b \sum_{i \in H(k)} \dfrac{(x_k - x_i)^2}{\sigma_{kl}^4} & k = l \\ -b I_{H(k)}(l) \dfrac{(x_k - x_i)^2}{\sigma_{kl}^4} & k \neq l \end{cases}$$
$$[F_{R_{XY}}]_{k,l} = \begin{cases} b \sum_{i \in H(k)} \dfrac{(x_k - x_i)(y_k - y_i)}{\sigma_{kl}^4} & k = l \\ -b I_{H(k)}(l) \dfrac{(x_k - x_i)(y_k - y_i)}{\sigma_{kl}^4} & k \neq l \end{cases}$$
$$[F_{R_{XZ}}]_{k,l} = \begin{cases} b \sum_{i \in H(k)} \dfrac{(x_k - x_i)(x_k - z_i)}{\sigma_{kl}^4} & k = l \\ -b I_{H(k)}(l) \dfrac{(x_k - x_i)(z_k - z_i)}{\sigma_{kl}^4} & k \neq l \end{cases}$$
$$[F_{R_{YY}}]_{k,l} = \begin{cases} b \sum_{i \in H(k)} \dfrac{(y_k - y_i)^2}{\sigma_{kl}^4} & k = l \\ -b I_{H(k)}(l) \dfrac{(y_k - y_i)^2}{\sigma_{kl}^4} & k \neq l \end{cases}$$
$$[F_{R_{YZ}}]_{k,l} = \begin{cases} b \sum_{i \in H(k)} \dfrac{(y_k - y_i)(z_k - z_i)}{\sigma_{kl}^4} & k = l \\ -b I_{H(k)}(l) \dfrac{(y_k - y_i)(z_k - z_i)}{\sigma_{kl}^4} & k \neq l \end{cases}$$
$$[F_{R_{ZZ}}]_{k,l} = \begin{cases} b \sum_{i \in H(k)} \dfrac{(z_k - z_i)^2}{\sigma_{kl}^4} & k = l \\ -b I_{H(k)}(l) \dfrac{(z_k - z_i)^2}{\sigma_{kl}^4} & k \neq l \end{cases} \tag{9}$$

Let $\hat{x}_i, \hat{y}_i, \hat{z}_i$ be the unbiased estimation of x_i, y_i, z_i, the trace of the covariance of the i_{th} location estimate is given by:

$$\begin{aligned} \sigma_i^2 &= tr\{cov_\theta(\hat{x}_i, \hat{y}_i, \hat{z}_i)\} \\ &= Var_\theta(\hat{x}_i) + Var_\theta(\hat{y}_i) + Var_\theta \hat{z}_i, \\ &\geq \Big[F_{R_{XX}} - (F_{R_{XY}} F_{R_{XZ}}) \begin{pmatrix} F_{R_{YY}} & F_{R_{YZ}} \\ F_{R_{YZ}} & F_{R_{ZZ}} \end{pmatrix}_{i,i}^{-1} \begin{pmatrix} F_{R_{XY}} \\ F_{R_{XZ}} \end{pmatrix} \Big] \\ &\quad + \Big[F_{R_{XY}} - (F_{R_{XY}} F_{R_{YZ}}) \begin{pmatrix} F_{R_{XX}} & F_{R_{XZ}} \\ F_{R_{XZ}} & F_{R_{ZZ}} \end{pmatrix}^{-1} \begin{pmatrix} F_{R_{XY}} \\ F_{R_{YZ}} \end{pmatrix} \Big]_{i,i}^{-1} \\ &\quad + \Big[F_{R_{ZZ}} - (F_{R_{XZ}} F_{R_{YZ}}) \begin{pmatrix} F_{R_{XX}} & F_{R_{XY}} \\ F_{R_{XY}} & F_{R_{YY}} \end{pmatrix}^{-1} \begin{pmatrix} F_{R_{XZ}} \\ F_{R_{YZ}} \end{pmatrix} \Big]_{i,i}^{-1} \end{aligned} \tag{10}$$

B. CRB FOR TOA POSITIONING WITH SENSOR WITH HIGHEST RSS (PATH OF LEAST RESISTANCE)

One metric to relate the precision of TOA and RSS established positioning approaches is their corresponding Cramer-Rao Lower Bounds (CRLB) [7]. The CRLB of a deterministic factor states a lower bound on the variance of its estimators.

For the operational rate, bandwidth and SNR employed in GPS systems this limit demonstrates that precision of a few meters is attainable if we can wait for some minutes. If we want to expand this technology to include body area networks, we have three issues (1) we require more accuracy to pinpoint objects contained in the body (2) we need to handle the extra path loss suffered by the signal while traveling into the tissue within practical measurement periods (3) we require procedures to handle potential multipath environments.

The distance power slope would significantly vary for different portions of the human flesh as presented in Fig. 13. Also, the distance measurement error for RSS comes to the order of the space between the transmitter and receiver, which would not be satisfactory for the millimeter level precision requisite inside the human body.

To verify this statement, we plotted the RSS from our simulations for each of the surface antenna locations shown in Fig. 3. This plot is shown in Fig. 11, and the gradient obtained from this plot came out to be 4.59, which is analogous to the model in published by NIST [18].

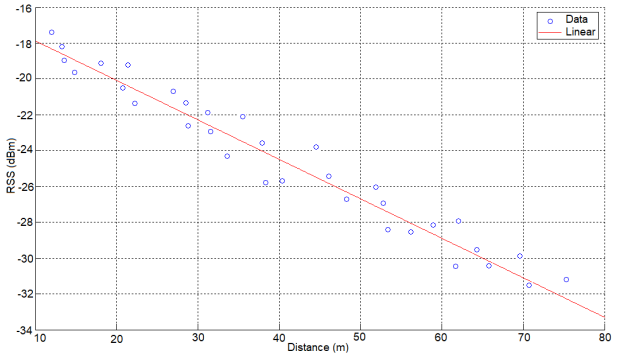

FIGURE 11. RSS vs. Distance plot for each sensor position.

The values plotted in Fig. 11 were then plugged into the NIST model and the distance measurement error for RSS was plotted. This plot is shown in Fig. 12. Notice that the errors obtained from TOA, shown in Fig. 9, are in the millimeter range and the highest value is 3.5 cm, while the ones shown in Fig. 12 are in cm, with the highest value being 5.1 cm. This confirms that ranging using RSS has larger errors than its TOA counterpart. To further establish this, if we plug in the values given in Fig. 12 into the path-loss model defined by Sayrafian-Pour *et al.* [18], at a distance of 50 cm, we can evaluate the CRLB on the variance of path-loss was in the range of 0.0699 and 0.427 dB;

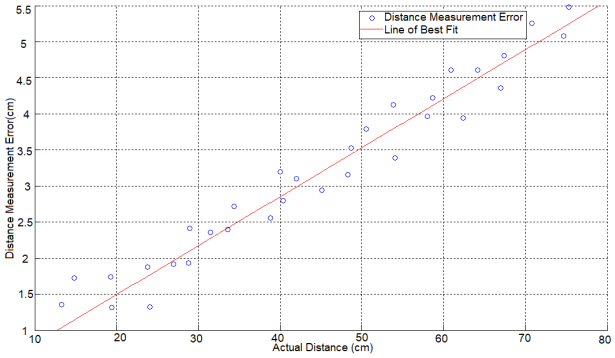

FIGURE 12. Distance Measurement Error from RSS for each sensor position.

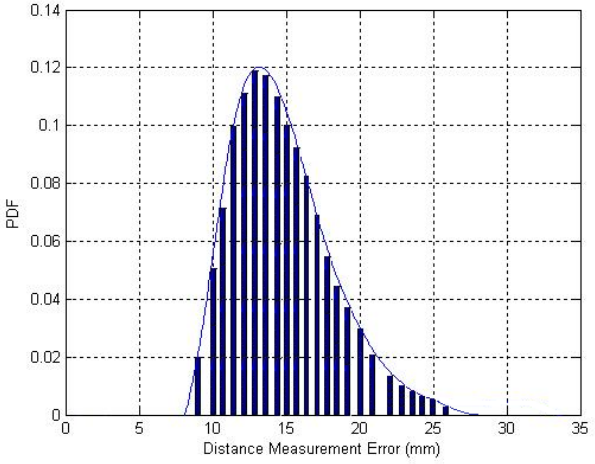

FIGURE 13. PDF of the Absolute Values of Distance Measurement Error from RSS for each sensor position.

while the CRLB on the variance of TOA using eq. (9) at the same distance came out to be 0.011388ns.

In this section, the variables to be calculated are the x, y and z positions of the pill, and a fresh array $\pi = [\pi_{01}, \ldots, \pi_{0N}]$ because not any of the N surface antennas have precise information of the time of arrival of the pulse it transmits. The Bayesian CRB [28] also known as Van trees inequality says that any approximation $\hat{\theta}$ must have an inaccuracy association matrix $R \in$ given by

$$R_\epsilon > F^{-1} = [F_\theta + F_O], \tag{11}$$

where $R_\epsilon = E[(\hat{\theta} - \theta)(\hat{\theta} - \theta)^T]$, and F_θ and F_P will be the FIM and the previous data matrix accordingly, given by eq. (12).

$$\begin{aligned} F_\theta &= -E[\nabla_\theta(\nabla)_\theta \ln f(p_{i,j}|\theta)^T], \\ F_p &= -E[\nabla_\theta(\nabla_\theta) \ln f(\theta)^T], \end{aligned} \tag{12}$$

where $p_{i,j}$ would be the dual-directional impulse response array. The previous data matrix F_P is given in eq. (12).

$$F_P = \text{diag}[0_n^T, 0_n^T.0_n^T, \frac{1_N^T}{\sigma_n^2}] \tag{13}$$

where 0_n would be an n-length array of zeros and 1_N represents an array of length N consisting of ones, while $\bar{\sigma}_\pi^2$ would be the variance of the random variable π_{0i} (the time of arrival 1 cm away from the pill i) that is supposed to have an i.i.d Gaussian probability distribution for each surface antenna i.

We represent the dual-directional measurements $P_{i,j}$ and $P_{j,I}$ by the array $p_{i,j} = [P_{i,j}P_{j,i}]$ as a dual-variable Gaussian with an average of $u_{i,j}$ and a variance of $C_{i,j}$, where

$$u_{i,j} = \begin{bmatrix} \pi_{0j} - 10x \log_{10} \dfrac{|r_i - r_j|^2}{\triangle_u^2} \\ \pi_{0i} - 10x \log_{10} \dfrac{|r_i - r_j|^2}{\triangle_u^2} \end{bmatrix} \tag{14}$$

$$C_{i,j} = \sigma_{dB}^2 \begin{bmatrix} 1 & \rho \\ \rho & 1 \end{bmatrix} \tag{15}$$

where α denotes the time of arrival exponent, and ρ would be the association constant among the dual-directional responses, $0 \leq \rho \leq 1$. For the sake of simplicity we convert the dual-directional response array $p_{i,j}$ to an orthogonal matrix A using the following derivation:

$$\begin{aligned} \tilde{\rho}_{i,j} &= Ap_{i,j}, \\ A &= \begin{bmatrix} 1 & 1 \\ 1 & -1 \end{bmatrix} \end{aligned} \tag{16}$$

Such a full rank transformation of measurement does not change the Fisher information. For simplicity of notation, we denote $\tilde{p}_{i,j} = [\bar{p}_{i,j}, p_{i,j}^{\triangle}]^T$, where $\bar{p}_{i,j}$ corresponds to the average of the two measurements and $p_{i,j}^{\triangle}$ corresponds to the difference between two measurements. After some mathematical analysis, it can be seen that $\bar{p}_{i,j}$ has a mean $\bar{u}_{i,j}$ and covariance $\bar{c}$ and $p_{ij}^{\triangle}$ has a mean $u_{ij}^{\triangle}$ and covariance $c^{\triangle}$ as given below

$$\begin{aligned} baru_{ij} &= \pi_{0j} + \pi_{0i} - 10x \log_1 0 \frac{|r_i - r_j|^2}{\triangle_0 2}, \\ \bar{c} &= \frac{(1+\rho)\sigma_{dB}^2}{2} I_{3n+N}, \\ u_{ij}^{\triangle} &= \frac{\pi_{0j} - \pi_{0i}}{2}, \\ c^{\triangle} &= \frac{(1-\rho)\sigma_{dB}^2}{2} I_{3n+N}, \end{aligned} \tag{17}$$

where I_{3n+N} is $3n + N \times 3n + N$ identity matrix and $\bar{u}$ and $y^{\triangle}$ are the mean values for the sum and difference of measurements respectively for all measured pairs,

$$\begin{aligned} \bar{u} &= [\bar{u}_{i_1,j_1}, \ldots, \bar{u}_{i_n,j_n}]^T, \\ u^{\triangle} &= [u_{i_1,j_1}^{\triangle}, \ldots, u_{i_N,j_N}^{\triangle}], \end{aligned} \tag{18}$$

where $i_1; j_1; \ldots; i_N, j_N$ corresponds to each unique pair. A pair makes measurement if they are in the measurement range of each other. Here we assume that the measurement rangeis infinite (i.e., every sensor can do measurements with every other sensor). The Fisher information matrix F_θ given by eq. (12) can be split into two sub matrices F_θ and $F_\theta^{\triangle}$

corresponding to sum and difference measurements due to their independence.

$$F_\theta = \bar{F}_\theta + F_\theta^\Delta. \tag{19}$$

The FIM of a vector of multivariate Gaussian measurements with mean $l(h)$ and covariance C is given by [24]

$$\begin{aligned} F_\theta &= [\nabla_\theta \mu(\theta)]^T C^{-1} [\nabla_\theta \mu(\theta)], \\ &= \begin{bmatrix} F_{R_{XX}} & F_{R_{XY}} & F_{R_{XZ}} & F_{R_{X\pi}} \\ F_{R_{YX}} & F_{R_{YY}} & F_{R_{YZ}} & F_{R_{Y\pi}} \\ F_{R_{ZX}} & F_{R_{ZY}} & F_{R_{ZZ}} & F_{R_{Z\pi}} \\ F_{R_{\pi X}} & F_{R_{\pi Y}} & F_{R_{\pi Z}} & F_{R_{\pi\pi}} \end{bmatrix}. \end{aligned} \tag{20}$$

From eq. 19 we have,

$$\begin{aligned} \bar{F}_\theta &= [\nabla_\theta \bar{\mu}(\theta)]^T C^{-1} [\nabla_\theta \bar{\mu}(\theta)], \\ &= \begin{bmatrix} \bar{F}_{R_{XX}} & \bar{F}_{R_{XY}} & \bar{F}_{R_{XZ}} & \bar{F}_{R_{X\pi}} \\ \bar{F}_{R_{YX}} & \bar{F}_{R_{YY}} & \bar{F}_{R_{YZ}} & \bar{F}_{R_{Y\pi}} \\ \bar{F}_{R_{ZX}} & \bar{F}_{R_{ZY}} & \bar{F}_{R_{ZZ}} & \bar{F}_{R_{Z\pi}} \\ \bar{F}_{R_{\pi X}} & \bar{F}_{R_{\pi Y}} & \bar{F}_{R_{\pi Z}} & \bar{F}_{R_{\pi\pi}} \end{bmatrix}, \end{aligned} \tag{21}$$

$$\begin{aligned} \bar{F}_\theta^\Delta &= [\nabla_\theta \mu^\Delta(\theta)]^T C^{-1} [\nabla_\theta \mu^\Delta(\theta)], \\ &= \begin{bmatrix} \bar{F}^\Delta_{R_{XX}} & \bar{F}^\Delta_{R_{XY}} & \bar{F}^\Delta_{R_{XZ}} & \bar{F}^\Delta_{R_{X\pi}} \\ \bar{F}^\Delta_{R_{YX}} & \bar{F}^\Delta_{R_{YY}} & \bar{F}^\Delta_{R_{YZ}} & \bar{F}^\Delta_{R_{Y\pi}} \\ \bar{F}^\Delta_{R_{ZX}} & \bar{F}^\Delta_{R_{ZY}} & \bar{F}^\Delta_{R_{ZZ}} & \bar{F}^\Delta_{R_{Z\pi}} \\ \bar{F}^\Delta_{R_{\pi X}} & \bar{F}^\Delta_{R_{\pi Y}} & \bar{F}^\Delta_{R_{\pi Z}} & \bar{F}^\Delta_{R_{\pi\pi}} \end{bmatrix}. \end{aligned} \tag{22}$$

The calculations of the discrete components of the matrix are comparable to eq. (9), and presented in [29].

V. ESTABLISHING THE ACCURACY OF THE ANSYS HFSS SOLVER

While previous studies [30] have attempted to use FDTD based 3D simulation methods to approximate TOA characteristics, in principle the FEM technique is established as more precise due to its use of tetrahedral meshes instead of a rectangular grid. An example of modelling wideband channel characteristics using the FEM technique in Ansys HFSS has been described in [31]. Real-life experiments were first conducted, whereby surface-to-surface measurements were taken, and then compared to their corresponding FEM simulations. Both in actual measurements and software simulations, two dipoles with 900MHz as their center frequency were placed 50cm apart (Fig. 14 (a)) and their channel parameters were plotted, using a network analyzer, over a bandwidth of 100MHz. This plot was then used to find the impulse response using the chirp z-transform function in Matlab. Next, a person with height 172cm and weight 156lbs was positioned between the two antennas (Fig. 14(b)). Additionally, a human body model with similar characteristics was placed in the HFSS simulation environment, between the two antennas (Fig. 15). The impulse response for this new channel was also plotted in the same way. The comparative results are shown in Fig. 16. The side faces of the radiation box in the HFSS simulations were assigned concrete as their material and the front and back faces were assigned the radiation boundary to imitate the environment of the lab.

FIGURE 14. Measurement setup (a) with body (b) without body.

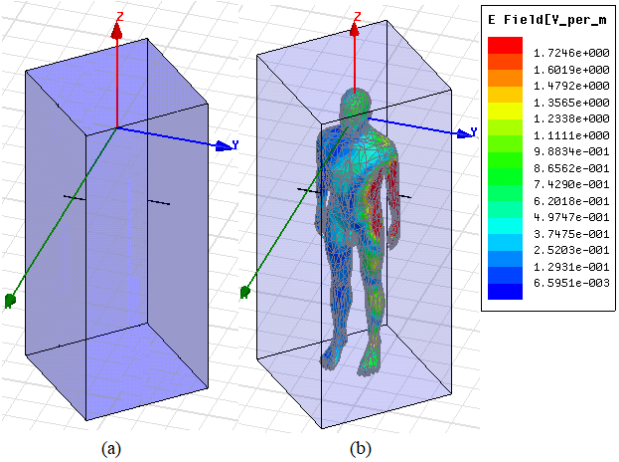

FIGURE 15. Ansoft HFSS TM simulation setup (a) without body (b) with body and electric field plot. The two horizontal black lines represent the dipoles.

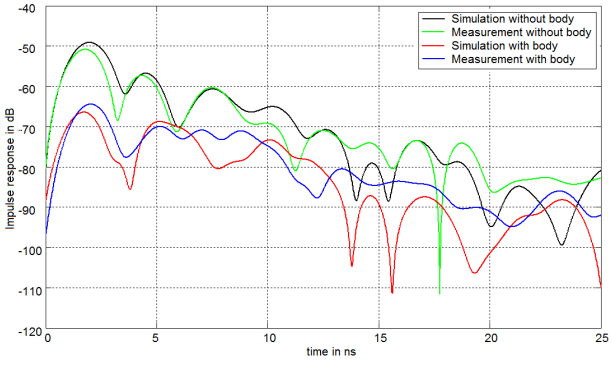

FIGURE 16. Impulse response obtained from the two simulated and measured channels.

From the measurement taken without the body, the TOA of the first path was calculated to be 1.70ns, which roughly translates to about 51cm - an error of 1cm from the actual distance. The same value from the HFSS simulation equals 1.95ns, which in turn translates to 58cm, indicating an error of about 7cm from the measurement. The TOA of the first path from measurements taken with the body computed as 2.07ns, translating into 60cm, which means that on average,

the human body would slow down the signal enough to cause a 9cm offset in the measurements. But the simulation with the body shows that the TOA of the first path is 2.00ns, again an offset of about 9cm from the measurements; showing a good correlation between measurements and simulations.

From Figure 4.14, the rms delay spread of the first three paths for the measurements without the body is 4.12ns and the same value for the simulation without the body is 3.97ns; a difference of just 0.15ns. When the body was added to the measurement setup, the rms delay spread was 3.79ns, the same value for the simulation with the body corresponds to 3.32ns; an error of about 0.47ns. Hence, it is shown using rms delay spread that the results obtained from the HFSS simulation are very close to those obtained from the actual measurements. This leads us to conclude that FEM is an effective means to simulate the wideband profile of a human body channel.

VI. CONCLUSION

This paper continues from the study conducted in the 2014 comparative evaluation of RSS and TOA by Ye *et al.* [32]. In that publication, the HFSS 3D model was only used to import the human body parts in order to trace the path of the capsule in a separate image processing software. In the experiments conducted in this study, we use the FEM technique available in the HFSS software locally to perform EM simulations between a fixed pill location and various external sensor locations on a 3D array. Furthermore, the CRLB derived in that study are used to establish the accuracy of RSS, while this study aims to use these functions for TOA calculations.

In this study, we examined the prospective precision constraints for TOA and cooperation based on path-of least resistance (received signal strength after shadow fading) positioning of an endoscopy pill traveling down the human digestive system. We confirmed the likelihood of accomplishing a mean positioning error of 50 mm in the gastrointestinal system. We also confirmed that no more than 10 receivers on the surface of the human body are required to accomplish sufficient positioning precision for pill-based endoscopy. Software model results using Ansys HFSS revealed that accumulating the quantity of surface antennas on the body would have higher effect on the general positioning accuracy. This is also practical, as we only use one pill to perform capsule endoscopy, but we can put multiple sensors on the surface. We also studied the consequence of arbitrariness in impulse response on the positioning precision. In conclusion and keeping real-world concerns in consideration, we make the inference that cooperating surface sensors, using RSS to determine shadow fading, and then determining the location using time of arrival of a pulse transmitted from the capsule will give us the best chance of accurate localization.

ACKNOWLEDGEMENTS

The authors would like to express their acknowledgements to Dr. Yishuang Geng, Dr. Kaveh Ghaboosi, Ruijun Fu, Dr. Nayef Alsindi and other colleagues in CWINS lab in preparing of this paper. And Dr. Tim Wig of Intel Corp. for helping with the computational resources needed for this paper.

REFERENCES

[1] G. Iddan, G. Meron, A. Glukhovsky, and P. Swain, "Wireless capsule endoscopy," *Nature*, vol. 405, no. 6785, p. 417, May 2000.

[2] J. Lee, J. Oh, S. K. Shah, X. Yuan, and S. J. Tang, "Automatic classification of digestive organs in wireless capsule endoscopy videos," in *Proc. ACM Symp. Appl. Comput.*, Seoul, South Korea, Mar. 2007, pp. 1041–1045.

[3] M. Frisch, A. Glukhovsky, and D. Levy, "Array system and method for locating an *in vivo* signal source," U.S. Patent US 6 904 308 B2, Jun. 7, 2005.

[4] D. Fischer, R. Schreiber, D. Levi, and R. Eliakim, "Capsule endoscopy: The localization system," *Gastrointestinal Endoscopy Clinics*, vol. 14, pp. 25–31, Jan. 2004.

[5] R. Kuth, J. Reinschke, and R. Rockelein, "Method for determining the position and orientation of an endoscopy capsule guided through an examination object by using a navigating magnetic field generated by means of a navigation device," U.S. Patent Application No. 11/481 935, Feb. 15, 2007.

[6] M. Kawasaki and R. Kohno, "A TOA based positioning technique of medical implanted devices," in *Proc. Int. Symp. Med. Inf. Commun. Technol.*, Montreal, Canada, Feb. 2009, pp. 1–5.

[7] C. Hu, M.-Q. H. Meng, and M. Mandal, "Efficient magnetic localization and orientation technique for capsule endoscopy," *Int. J. Inf. Acquisition*, vol. 2, no. 1, pp. 22–36, Mar. 2005.

[8] G. Bao, K. Pahlavan, and L. Mi, "Hybrid localization of microrobotic endoscopic capsule inside small intestine by data fusion of vision and RF sensors," *IEEE Sensors J.*, vol. 15, no. 5, pp. 2669–2678, May 2015.

[9] Y. Geng and K. Pahlavan, "On the accuracy of RF and image processing based hybrid localization for wireless capsule endoscopy," in *Proc. IEEE Wireless Commun. Netw. Conf. (WCNC)*, New Orleans, LA, USA, Mar. 2015, pp. 452–457.

[10] G. Ciuti, P. Valdastri, A. Menciassi, and P. Dario, "Robotic magnetic steering and locomotion of microsystems for diagnostic and surgical endoluminal procedures," *Robotica*, vol. 28, no. 2, pp. 199–207, 2009.

[11] G. Ciuti, A. Menciassi, and P. Dario, "Capsule endoscopy: From current achievements to open challenges," *IEEE Rev. Biomed. Eng.*, vol. 4, pp. 59–72, Oct. 2011.

[12] S. Thomas, "Smartpill redefines 'noninvasive,'" *Buffalo Phys.*, vol. 40, no. 3, pp. 13–14, 2006.

[13] H. Jacob, D. Levy, R. Shreiber, A. Glukhovsky, and D. Fischer, "Localization of the given M2A ingestible capsule in the given diagnostic imaging system," *Gastrointestinal Endoscopy*, vol. 55, no. 5, p. AB135, 2002.

[14] T. Ito, D. Anzai, and J. Wang, "Performance comparison between TOA- and RSSI-based localization methods for wireless capsule endoscopy systems," in *Proc. Int. Symp. Med. Inf. Commun. Technol.*, Kamakura, Japan, Mar. 2015, pp. 139–143.

[15] S. Jeong, J. Kang, K. Pahlavan, and V. Tarokh, "Fundamental limits of TOA/DOA and inertial measurement unit-based wireless capsule endoscopy hybrid localization," *Int. J. Wireless Inf. Netw.*, vol. 24, no. 2, pp. 169–179, 2017.

[16] L. Wang, C. Hu, L. Tian, M. Li, and M. Q.-H. Meng, "A novel radio propagation radiation model for location of the capsule in GI tract," in *Proc. IEEE Int. Conf. Robot. Biomimetics (ROBIO)*, Guilin, China, Sep. 2009, pp. 2332–2337.

[17] K. Arshak and F. Adepoju, "Adaptive linearized methods for tracking a moving telemetry capsule," in *Proc. IEEE Int. Symp. Ind. Electron.*, Vigo, Spain, Jun. 2007, pp. 2703–2708.

[18] K. Sayrafian-Pour, W.-B. Yang, J. Hagedorn, J. Terrill, and K. Y. Yazdandoost, "A statistical path loss model for medical implant communication channels," in *Proc. IEEE 20th Int. Symp. Pers., Indoor Mobile Radio Commun.*, Tokyo, Japan, Sep. 2009, pp. 2995–2999.

[19] Y. Wang, R. Fu, Y. Ye, U. Khan, and K. Pahlavan, "Performance bounds for RF positioning of endoscopy camera capsules," in *Proc. IEEE Top. Conf. Biomed. Wireless Technol., Netw., Sens. Syst.*, Phoenix, AZ, USA, Jan. 2011, pp. 71–74.

[20] N. Alsindi and K. Pahlavan, "Cooperative localization bounds for indoor ultra-wideband wireless sensor networks," *EURASIP J. Adv. Signal Process.*, vol. 2008, Jan. 2008, Art. no. 852509.

[21] N. Bargshady, N. A. Alsindi, K. Pahlavan, Y. Ye, and F. O. Akgul, "Bounds on performance of hybrid WiFi-UWB cooperative RF localization for robotic applications," in *Proc. IEEE Int. Symp. Pers., Indoor Mobile Radio Commun. Workshops*, Instanbul, Turkey, Sep. 2010, pp. 277–282.

[22] *ANSYS Full-Wave Electromagnetic Filed Simulation*. Accessed: Apr. 7, 2017. [Online]. Available: http://www.ansys.com/products/electronics/ansys-hfss

[23] A. Nafchi, S. T. Goh, and S. R. Zekavat, "Circular arrays and inertial measurement unit for DOA/TOA/TDOA-based endoscopy capsule localization: Performance and complexity investigation," *IEEE Sensors J.*, vol. 14, no. 11, pp. 3791–3799, Nov. 2014.

[24] N. Patwari and A. O. Hero, III, "Signal strength localization bounds in ad hoc and sensor networks when transmit powers are random," in *Proc. IEEE Workshop Sensor Array Multichannel Process.*, Waltham, MA, USA, Jul. 2006, pp. 299–303.

[25] H.-B. Li, K. Y. Yazdandoost, and B. Zhen, *Wireless Body Area Network* (Series in Information Science and Technology). Gistrup, Denmark: River Publishers, 2010.

[26] N. Patwari, A. O. Hero, M. Perkins, N. S. Correal, and R. J. O'Dea, "Relative location estimation in wireless sensor networks," *IEEE Trans. Signal Process.*, vol. 51, no. 8, pp. 2137–2148, Aug. 2003.

[27] J. Bulat *et al.*, "Data processing tasks in wireless GI endoscopy: Image-based capsule localization & navigation and video compression," in *Proc. Int. Conf. IEEE Eng. Med. Biol. Soc.*, Lyon, France, Aug. 2007, pp. 2815–2818.

[28] S. M. Kay, *Fundamentals of Statistical Signal Processing: Estimation Theory*. Upper Saddle River, NJ, USA: Prentice-Hall, 1993.

[29] P. Swar, Y. Ye, K. Ghaboosi, and K. Pahlavan, "On effect of transmit power variance on localization accuracy in wireless capsule endoscopy," in *Proc. IEEE Wireless Commun. Netw. Conf.*, Shanghai, China, Apr. 2012, pp. 2119–2123.

[30] M. Zhou and K. Pahlavan, "On the accuracy of in-body TOA ranging inside the gastrointestinal tract using carrier frequency," in *Proc. IEEE Wireless Telecommun. Symp.*, New York, NY, USA, Apr. 2015, pp. 1–5.

[31] F. Askarzadeh, Y. Ye, U. Khan, K. Pahlavan, and S. Makarov, "Computational methods for localization," in *Handbook of Position Location—Theory, Practice and Advances*, 1st ed. Marblehead, MA, USA: Wiley, ch. 5, pp. 137–172.

[32] Y. Ye, K. Pahlavan, G. Bao, P. Swar, and K. Ghaboosi, "Comparative performance evaluation of RF localization for wireless capsule endoscopy applications," *Int. J. Wireless Inf. Netw.*, vol. 21, no. 3, pp. 208–222, Sep. 2014.